Coupling between ice flow and subglacial hydrology enhances marine ice-sheet retreat

George Lu[1] and Jonathan Kingslake[1]

[1]Lamont-Doherty Earth Observatory of Columbia University, Palisades, NY, USA

Correspondence: George Lu (george.lu@columbia.edu)

Abstract. Ice-sheet models used to predict sea-level rise often neglect subglacial hydrology. However, theory and observations suggest that ice flow and subglacial water flow are bidirectionally coupled: ice flow and geometry affects hydraulic potential, hydraulic potential modulates basal shear stress via the basal water pressure, and ice flow advects the subglacial drainage system. This coupling could impact rates of ice mass change, but remains poorly understood. We combine a channelized subglacial hydrology model with a depth-integrated marine-ice-sheet model, incorporating each component of the coupling listed above, which yields a set of differential equations that we solve using a finite-difference, implicit time-stepping approach. We conduct a series of experiments with this model, using either bidirectional or unidirectional coupling. These experiments generate steady-state profiles of channel cross-sectional area, channel flow rate, channel effective pressure, ice thickness, and ice velocity. We discuss how the steady-state profiles shape one another, resulting in the effective pressure reaching a local maximum in a region near the grounding line. We also describe the impact of bidirectional coupling on the transient retreat of ice sheets through a comparison of our coupled model with ice-flow models that have imposed static basal conditions. We find that including coupled subglacial hydrology leads to grounding-line retreat that is virtually absent when static basal conditions are assumed. This work highlights the role time-evolving subglacial drainage may have in ice-sheet change and informs efforts to include it in ice-sheet models.

1 Introduction

The Ice-Sheet Model Intercomparison for CMIP6 (ISMIP6) predicts between 7.8 and 30.0 cm of sea-level-equivalent ice-mass loss from Antarctica by 2100 under the Representative Concentration Pathway 8.5 scenario (Seroussi et al., 2020). This wide range of predictions for the same forcing scenario is associated with various uncertainties within and differences between the ice-sheet models. A significant source of uncertainty is a limited understanding of how evolving subglacial hydrology could influence ice-sheet mass loss (Seroussi et al., 2020; De Fleurian et al., 2018; Flowers, 2015). A common approach to capturing the effect of hydrology on ice dynamics in ice-sheet models is to use measured surface velocities to invert for a spatially varying basal friction parameter (Arthern and Gudmundsson, 2010; Morlighem et al., 2013; Arthern et al., 2015; Lipscomb

et al., 2021). This parameter encompasses all bed properties relevant for basal shear stress, including subglacial hydrology.
25 Usually, this parameter remains static in time during simulations and does not evolve with changes in hydrology or basal water
pressure (e.g., Lipscomb et al., 2021; Gudmundsson et al., 2019; Arthern and Williams, 2017). However, subglacial hydrology
does evolve, and variations in basal water pressure have been linked to changes in ice dynamics (Fountain and Walder, 1998;
Bartholomew et al., 2010; Clarke, 2005; Bindschadler, 1983).

Another way to represent subglacial hydrology in ice-sheet models is with simple parameterizations or with simple models
30 (Kazmierczak et al., 2022; McArthur et al., 2023). These relate basal water pressure to the depth of the bed below sea level (e.g.,
Tsai et al., 2015) or the hydrological connectivity to the ocean (e.g., Leguy et al., 2014), or use simple hydrology models to
estimate the depth of subglacial water (e.g., Le Brocq et al., 2009) or the till pressure (e.g., Bueler and Brown, 2009). However,
ice-sheet sensitivity to subglacial hydrology varies greatly based on the parameterization or simple model used. Kazmierczak
et al. (2022) showed that the range of sea-level-rise (SLR) predictions associated with these different parameterizations in a
35 single ice-sheet model is similar in magnitude to the difference in SLR predictions between models used in ISMIP6 (Seroussi
et al., 2020). Additionally, some of these simple parameterizations are likely not representative of the entire ice-sheet bed, and
are only valid near the grounding line (Kazmierczak et al., 2022; Leguy et al., 2014).

Given that parameterizations of time-varying subglacial hydrology are often highly simplified, while basal friction parame-
ters determined through inversion techniques do not evolve in time, we explore an alternative approach to examine the effect
40 of evolving hydrology on ice-sheet retreat. We couple a physics-based subglacial hydrology model with an ice-sheet model,
using a simple, one-dimensional approach. Our model avoids some of the common simple parameterizations for subglacial
hydrology and allows the hydrology and the ice sheet to evolve dynamically in a coupled way. We use this model to examine
how the coupling operates and investigate the assumption of holding basal friction parameters static in transient simulations.

Our work differs from previous coupled models of ice flow and hydrology by considering a marine-terminating setting, using
45 higher-order ice flow physics than some models, and using a simpler hydrology model. For example, Kingslake and Ng (2013)
and Arnold and Sharp (2002) coupled multi-element subglacial hydrology models, including channels and distributed linked
cavities, to simplified ice-flow models, using an ice slab and the shallow ice approximation, respectively. In contrast, we use a
higher-order ice-flow model including longitudinal stresses. Several other models (Pimentel and Flowers, 2010; Hewitt, 2013;
Hoffman and Price, 2014; Gagliardini and Werder, 2018) couple similar multi-element hydrology systems to higher-order ice
50 flow models to study land-terminating glaciers. In contrast, we model marine-terminating glaciers. Finally, rather than using
the multi-element hydrology models considered in other studies, we model a single, one-dimensional channel.

Application to marine-terminating glaciers necessitates a set of three couplings between the ice and hydrology models. The
first is a sliding law that depends on effective pressure. This is motivated by the idea that the water pressure underneath the ice
sheet can modulate the basal shear stress (Iken and Bindschadler, 1986). The second is allowing the ice geometry to modulate
55 the basal hydraulic gradient (Fowler, 1999). The third is allowing the velocity of the ice to advect the drainage system (Drews
et al., 2017). These points of coupling are illustrated by the solid lines in Fig. 1.

We consider marine-terminating ice due to its importance for future ice-sheet mass balance, and a channelized drainage sys-
tem because observations and modeling suggest that there exist large, persistent channels underneath portions of the Antarctic
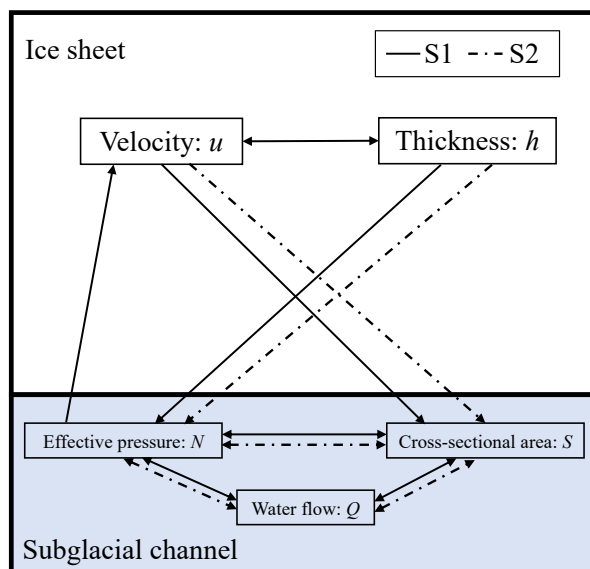
Figure 1. Points of coupling illustrated for our full coupled model (solid lines; S1), and a model with imposed ice geometry and velocity (dash-dot lines; S2).

Ice Sheet (Le Brocq et al., 2013; Drews et al., 2017; Dow et al., 2022). This motivates our choice to represent the hydrology
60   system as a subglacial channel.

Section 2 describes our model and a set of steady-state and transient numerical experiments. Section 3 presents the results of these experiments. A key result is that the coupling between water and ice flow generates a region of relatively high effective pressure upstream of the grounding line in steady-state experiments. The transient experiments show the consequences of this high effective pressure region for simulated retreat. Section 4 discusses and explains these results with the aid of a reduced
65   version of the hydrology model and Section 5 draws conclusions about how these findings may apply to real systems.

2   Methods

Here, we describe the models of ice flow, basal sliding, and subglacial hydrology included in our coupled model. We also describe our numerical experiments. We first conduct a suite of steady-state experiments to understand the effects of parameter choices. We then examine a simulation in more detail to investigate the resulting effective pressure profiles. Next, we illustrate
70   the importance of coupling for ice sheet retreat through a set of transient experiments.

2.1   Ice dynamics

The ice-flow component of our model describes a two-dimensional, symmetric, shallow, marine ice sheet (e.g., Schoof, 2007; Muszynski and Birchfield, 1987; MacAyeal, 1989). It is depth-integrated and assumes rapid sliding, and its full derivation is

described by Muszynski and Birchfield (1987). We use this model because it is one of the simplest models that accounts for

75 longitudinal stresses, which are important near the grounding line. Mass and momentum balance are described by

$$\frac{\partial h}{\partial t} + \frac{\partial (hu)}{\partial x} = a, \tag{1}$$

$$\frac{\partial}{\partial x}\left[2A^{-1/n}h\left|\frac{\partial u}{\partial x}\right|^{1/n-1}\frac{\partial u}{\partial x}\right] - \tau_b - \rho_i g h \frac{\partial (h-b)}{\partial x} = 0, \tag{2}$$

where h is the ice thickness, u is the vertically uniform horizontal ice velocity, x is distance from the ice divide, t is time, a is the ice-equivalent accumulation rate, τ_b is the basal shear stress, ρ_i is the density of ice, g is the acceleration due to gravity, n

80 is the Glen's law exponent, and A is a depth-averaged Glen's law coefficient. We use boundary conditions described by Schoof (2007). At the divide ($x = 0$) we impose symmetry, $\frac{\partial (h-b)}{\partial x} = 0$ and $u = 0$, and at the grounding line ($x = x_g$) we impose flotation $\rho_i h = \rho_w b$ and a stress balance based on coupling to a downstream ice shelf,

$$2\bar{A}^{-1/n}h\left|\frac{\partial u}{\partial x}\right|^{1/n-1}\frac{\partial u}{\partial x} = \frac{1}{2}\rho_i\left(1 - \frac{\rho_i}{\rho_w}\right)gh^2, \tag{3}$$

where ρ_w is the density of water. This stress condition accounts for flotation and the lack of basal shear stress at x_g, which is

85 consistent with the assumption described later that effective pressure is zero at the grounding line. The mass balance (Eq. 1) dictates that thickness changes in the ice are due to the imbalance between the accumulation rate a and the flux divergence. The momentum balance (Eq. 2) describes the balance between the longitudinal stress (first term), vertical shear stress (second term), and driving stress (third term). The hydrology influences the ice dynamics by modulating the basal shear stress, which is represented by an effective-pressure-dependent sliding law.

2.2 Sliding laws

Different choices of sliding law for representing the basal shear stress τ_b yield different behaviors in ice-sheet models, especially near the grounding line (e.g., Brondex et al., 2017; Tsai et al., 2015; Barnes and Gudmundsson, 2022). Classically, models use a power law (also known as a Weertman law) to describe the relationship between τ_b and the sliding velocity (Weertman, 1957):

95 $$\tau_b = C_W u^m, \tag{4}$$

where m is usually related to the exponent in Glen's flow law, n (Paterson, 1994), and C_W is a basal friction parameter that describes the bed properties. Typically, $m = \frac{1}{n} = \frac{1}{3}$ (e.g., Weertman, 1974; Schoof, 2007). Equation (4) does not explicitly consider the dependence that τ_b can have on the effective pressure, N, defined as the ice overburden pressure minus the subglacial water pressure.

100 The first N-dependent sliding law we adopt is an adjusted power law proposed by Budd et al. (1979):

$$\tau_b = C_B N^q u^m, \tag{5}$$

where C_B is another friction parameter with the subscript used to distinguish it from C_W, and q is a positive constant. Present models with this style of sliding law (which we refer to as a Budd sliding law) typically use a value of $q = 1$ (Brondex

et al., 2017). One drawback associated with this sliding law is that the inclusion of N can result in large, nonphysical stresses

105   (Brondex et al., 2017).

The second N-dependent sliding law we adopt is a regularized-Coulomb law (Helanow et al., 2021; Schoof, 2005):

$$\tau_b = C_C N \left(\frac{u}{u + A_s C_C^n N^n} \right)^{1/n},$$

(6)

where A_s and C_C are parameters describing the bed that Helanow et al. (2021) use as fitting parameters. Sliding laws in this

form have been used to represent sliding with cavitation on hard beds and sliding over deformable glacial till (e.g., Schoof,

110   2005; Zoet and Iverson, 2020; Helanow et al., 2021). In the limit of high N, this law behaves like a power law, Eq. (4). In the

limit of low N (typical near the grounding line), Eq. (6) reduces to a Coulomb plastic sliding law, $\tau_b \approx C_C N$, and does not

have a strong dependence on ice velocity.

2.3   Subglacial hydrology

Our hydrology model describes the evolution of a subglacial channel and the balances of mass, momentum, and energy in the

115   channel, respectively, as follows:

$$\frac{\partial S}{\partial t_h} = \frac{m}{\rho_i} - K_0 S N^3 - u \frac{\partial S}{\partial x},$$

(7)

$$\frac{\partial S}{\partial t_h} + \frac{\partial Q}{\partial x} = \frac{m}{\rho_w} + M,$$

(8)

$$\psi + \frac{\partial N}{\partial x} = f \rho_w g \frac{Q|Q|}{S^{8/3}},$$

(9)

$$mL = Q \left(\psi + \frac{\partial N}{\partial x} \right).$$

(10)

120   S is the channel cross-sectional area, N is the effective pressure, Q is the channel discharge, M is a constant and uniform

supply term, m is the melt rate, t_h is the time for the hydrology system (which we distinguish from t for convenience when

nondimensionalizing later), f is a hydraulic friction factor, K_0 is an ice flow parameter, and ψ is the basic hydraulic gradient.

The basic hydraulic gradient ψ is the hydraulic gradient that would exist if the water pressure in the channel were equal to the

ice overburden pressure p_i, which is approximated as $\rho_i g h$:

125   $$\psi = \rho_w g \frac{\partial b}{\partial x} - \rho_i g \frac{\partial h}{\partial x}.$$

(11)

We impose $N = 0$ at the grounding line because the water pressure under the ice is expected to approximately equal the ice

overburden pressure in this location. We also force a channel discharge boundary condition at the divide, where we maintain a

constant small influx Q_{in} (effectively a Neumann boundary condition on N).

This formulation is based on the modification by Fowler (1999) of the model for a one-dimensional subglacial channel from

130   Nye (1976), with the addition of an ice advection term $u \frac{\partial S}{\partial x}$ in Eq. (7), following Drews et al. (2017). Equation (7) shows

how the channel cross-sectional-area evolution $\frac{\partial S}{\partial t}$ grows with melt $\frac{m}{\rho_i}$ and closes with ice creep $K_0 S N^3$. The advection term

in Eq. (7) captures how ice sliding moves the roof of the channel over a given point on the channel floor. This is necessary

for a steady state to be reached, as we will explain in our results. Equation (8) balances the flux associated with evolution of the channel cross-sectional area, flux divergence along the channel, and water gained through either melt or additional

135　water sources represented by M. Equation (9) uses Manning's equation (e.g., Chow, 1959; Röthlisberger, 1972) to describe the pressure gradient necessary to drive a flux Q through a channel with a cross-sectional area S. Equation (10) details the assumption that all the energy dissipated by the turbulently flowing water is used locally to melt the channel walls.

　　The hydrology depends on the ice geometry and dynamics as the hydraulic gradient depends on the ice overburden pressure, which in turn depends on the ice thickness h, while the velocity of the ice u advects the subglacial channel, as described in Eq.

140　(7). The hydrology in turn determines the effective pressure N, which enters the sliding laws used in Eq. (2) and affects the flow of the ice sheet.

2.4　Nondimensionalization and Numerics

To aid in numerically solving these equations and to understand the scales of each term, we nondimensionalize them (see Appendix A for the full procedure). There are six unknowns (Q, N, S, h, u, m) and six equations, but for simplicity we

145　eliminate m between Eq. (7), (8) and (10), reducing this to five unknowns and five equations. The dimensionless forms of the model equations are:

$$\frac{\partial S'}{\partial t'_h} = \frac{|Q'|^3}{S'^{8/3}} - S'N'^3 - \beta u' \frac{\partial S'}{\partial x'}, \tag{12}$$

$$\frac{\partial Q'}{\partial x'} = \epsilon(r-1)\frac{|Q'|^3}{S'^{8/3}} + \epsilon\left(S'N'^3 + \beta u'\frac{\partial S'}{\partial x'}\right) + M', \tag{13}$$

$$\frac{\partial N'}{\partial x'} = \frac{1}{\delta}\left(\frac{Q'|Q|}{S'^{8/3}} - \psi'\right), \tag{14}$$

150　
$$\frac{\partial h'}{\partial t'} + \frac{\partial(h'u')}{\partial x'} = a', \tag{15}$$

$$\alpha \frac{\partial}{\partial x'}\left[h'\left|\frac{\partial u'}{\partial x'}\right|^{1/n-1}\frac{\partial u'}{\partial x'}\right] - \tau'_b - h'\frac{\partial(h'-b')}{\partial x'} = 0, \tag{16}$$

and the associated parameters are: $\beta \equiv \frac{t_{h0}}{t_0}$, $\epsilon \equiv \frac{x_0 m_0}{Q_0\rho_i}$, $r \equiv \rho_i/\rho_w$, $\delta \equiv \frac{N_0}{x_0\psi_0}$, and $\alpha \equiv \frac{2u_0^{1/2}}{\rho_i g A^{1/n} h_{g0} x_0^{1/n}}$.

τ'_b depends on the sliding law choice. Nondimensionalizing Eq. (5) gives

$$\tau'_b = N'u'^{1/n}, \tag{17}$$

155　while nondimensionalizing Eq. (6) gives

$$\tau'_b = \gamma N'\left(\frac{u'}{u'+N'^n}\right)^{1/n}, \tag{18}$$

with $\gamma \equiv \frac{CN_0 x_0}{\rho_i g h_{g0}^2}$. Dashes indicate dimensionless variables which can be returned to their dimensional forms by multiplying with their scale (e.g., $x = x_0 x'$). For clarity, we drop dashes for the remainder of the analysis; unless otherwise stated, all variables referred to are their dimensionless forms. Constants for the experiments detailed in the subsequent sections are found

160　in Table 2, while the resulting parameter and scale values are found in Table 3.

Regardless of the sliding law used we find that $\beta \ll 1$ (Table 3), because the time scale for the hydrology, t_{h0}, is about four orders of magnitude smaller than the time scale for the ice sheet, t_0; t_{h0} is on the order of months while t_0 is on the order of millennia. We interpret this as the hydrology being in a "quasi-steady" state, meaning that it quickly reaches a steady state for whatever conditions the ice imposes as the ice evolves. $\beta \ll 1$ implies that the ice advection term in Eq. (12) has minimal effect. Regardless, we retain that term in anticipation of it becoming important in cases when $\frac{\partial S}{\partial x}$ is large. Another insight stemming from these parameter values is that $\alpha \ll \gamma$ and $\alpha \ll 1$, which implies, for the regularized Coulomb and Budd cases, respectively, that the basal shear stress has a much larger impact on the ice-sheet force balance than the longitudinal stresses in Eq. (16). Regardless, to better represent the dynamics near the grounding line where the basal shear stress vanishes, we retain the longitudinal stress term.

To solve these equations, we apply the finite-difference approximation following Schoof (2007). The ice velocity and thickness grids are staggered and split into two segments, one with coarse resolution and another with fine resolution near the terminus. This split-grid approach is to preserve computational efficiency while properly resolving the stresses near the grounding line. The different grids used in our experiments are described in Table 1. To account for a moving grounding line, we apply a coordinate transformation (detailed in Appendix A) that allows for the "stretching" of the grids, also following Schoof (2007). The grounding-line position is implicitly determined at each time step through enforcing continuity of thickness at the junction between the two segments of each grid and imposing the flotation condition. For the hydrology equations, we use a uniform grid at an intermediate resolution. The hydrology equations also undergo the same coordinate stretching as the ice equations. In each iterative step, the effective pressure is linearly interpolated onto the velocity grid while both the velocity and ice thickness are linearly interpolated onto the hydrology grid. The spatial derivatives are approximated with centered differences, unless they are at the boundary and not addressed by a boundary condition, in which case we use one-sided differences. The time derivatives are solved with a backwards Euler method. The system of nonlinear discrete equations is solved iteratively with MATLAB's *fsolve* function. This solution method is based on code from Robel (2021), which he used to solve the model described by Schoof (2007).

2.5 Experimental design

Table 1 summarizes our suite of experiments. We conduct a series of steady-state simulations, followed by a series of transient simulations. In the sections below, we describe the detailed setup of these experiments.

2.5.1 Steady-state experiments

We run a suite of steady-state simulations by setting the time derivatives in the model equations to zero and solving the resulting system of equations. First, to test model sensitivity, we vary the following constants across 100 uniformly spaced values over ranges noted in the square brackets, while fixing the others: the depth-averaged flow law constant $A \in [0.1, 10] \times 10^{-25}$ $\text{s}^{-1}\text{Pa}^{-3}$, the accumulation rate $a \in [0.1, 10]$ m yr^{-1}, the additional water source term $M \in [0, 10] \times 10^{-4}$ m^2 s^{-1}, and the water flux at the divide $Q_{\text{in}} \in [0.001, 10]$ m^3 s^{-1}. Additionally, we examine the sensitivity to the sliding law parameters $C_C \in [0.1, 1]$ and $A_s \in [0.01, 100] \times 10^{-21}$ m s^{-1}Pa^{-3} for the version of the model using a regularized Coulomb law, and $C_B \in [3, 15]$

Table 1. Experiments

name	fixed ice shape/velocity (Y/N)	fixed hydrology (Y/N)	ice grid points	hydrology grid points	transience (Y/N)
sensitivity	N	N	coarse (95%): 100 fine (5%): 200	500	N
S1	N	N	3000	3000	N
S2	Y	N	3000	3000	N
T1	N	N	coarse (85%): 100 fine (15%): 600	1000	Y
T2	N	Y	coarse (85): 100 fine (15%): 600	1000	Y

$\mathrm{m}^{-1/3}\ \mathrm{s}^{1/3}$ for the version using a Budd sliding law. In this suite of experiments (referred to as "sensitivity" in Table 1), we

195 use a linear bed with a slope of 0.001, which slopes downwards in the direction of ice flow from a depth of 100 m below sea level at the divide ($x = 0$). We impose $Q_0 = 1\ \mathrm{m}^3\ \mathrm{s}^{-1}$, $h_0 = 1000$ m, and $x_0 = 100$ km, and all other scales are derived from these values. When held fixed, the constants follow the values in Table 2. For the ice grid, we use 100 points along 95% of the domain and resolve the remaining 5% with 200 points. The hydrology grid has a uniform spacing with 300 points. These grids were chosen to properly resolve the region near the grounding line while preserving computational efficiency.

200   Outside of this suite of steady-state experiments, we also run a set of experiments at a higher spatial resolution with a specific parameter combination to examine the model behavior in more detail. These specific runs are referred to as S1 and S2 (Table 1), and are represented by the lines in Fig. 1. The relevant parameter values, constants, and scales used are detailed in Tables 2 and 3. We maintain the same bed slope described above. For these experiments, we use uniform grids at a high resolution. We use 3000 grid points for the thickness, velocity, and hydrology grids. We use this finer grid to validate our grid spacing choices

205 from the larger suite of steady state experiments experiments.

   S1 consists of two steady-state experiments solving the full coupled model. S1.B uses a Budd sliding law (Eq. 5), while S1.C uses a regularized Coulomb sliding law (Eq. 6). We follow this nomenclature for the remaining experiments that use different sliding laws in our full coupled model. Note that although different sliding laws are used, the same points of coupling are preserved, hence the collective usage of "S1".

210   S2 describes a simplified scenario with an imposed ice geometry and velocity. We impose an ice sheet with a quadratic shape, with its thickness described by

$$h = 10^3 \times \left(\sqrt{\frac{2.5 \times 10^5 - x}{2.5 \times 10^5}} + 0.3838 \right)\ \mathrm{m}, \tag{19}$$

where $x \in [0, 2.5 \times 10^5]$ m. The grounding line is defined to be 250 km away from the divide, as that is approximately its location in our S1 results. The 0.3838 factor is to make sure that the ice thickness at the grounding line equals the flotation thickness.

Table 2. Constants used in model experiments S1, S2, T1, and T2

constant	description	value
A	depth-averaged Glen's law coefficient*	2.9×10^{-25} s^{-1}Pa^{-3}
A_s	Coulomb law ice rheology and bed morphology coefficient	2.26×10^{-21} m s^{-1}Pa^{-3}
a	accumulation rate	1 m yr^{-1}
C_C	Coulomb law fitting coefficient*	0.2
C_B	Budd law coefficient	7.624 m$^{-1/3}$ s$^{1/3}$
f	channel friction factor	0.07 m$^{-2/3}$ s^2
g	gravitational acceleration	9.81 m s^{-2}
K_0	flow parameter for inward ice deformation	1×10^{-24} s^{-1}Pa^{-3}
L	latent heat of fusion of water	3.3×10^5 J kg^{-1}
M	additional water supply along channel	1×10^{-5} m^2 s^{-1}
n	Glen's law exponent	3
Q_{in}	influx at divide	0.01 m^3 s^{-1}
ρ_i	density of ice	917 kg m^{-3}
ρ_w	density of water	1028 kg m^{-3}

*Note that for the transient experiments T1 and T2, we perturbed A from 0.9×10^{-25} s^{-1}Pa^{-3} to 2.9×10^{-25} s^{-1}Pa^{-3}, and used $C_C = 0.5$. We also used $M = 1 \times 10^{-6}$ m^2 s^{-1} and $Q_{\mathrm{in}} = 0.01$ m^3 s^{-1}.

215   This scenario also imposes a uniform velocity of about 91.6 m yr^{-1}, which is the scale u_0 from Experiments S1. These velocity and thickness values were selected to be the same order of magnitude as the results from the coupled experiments. We hold these velocity and thickness values constant and use them to solve only the hydrology equations for a steady state. Employing this one-directional coupling in this experiment will help us understand how ice geometry drives the hydrology. As illustrated in Fig. 1, imposing this ice geometry and velocity removes the point of coupling where the effective pressure modulates the

220 basal shear stress.

2.5.2 Transient experiments

We also perform two suites of of transient experiments with the full coupled model, which we call T1 and T2. Like the experiments in S1, this set of experiments uses both a Budd sliding law (T1.B, T2.B) and a regularized Coulomb sliding law (T1.C, T2.C).

225   For all transient experiments, we run the model to a steady state, then perturb the ice flow constant A, in Eq. (2). To instigate ice-sheet thinning and grounding-line retreat, we instantaneously increase A from 0.9×10^{-25} s^{-1}Pa^{-3} to 2.9×10^{-25} s^{-1}Pa^{-3}. This approach follows Schoof (2007) and is equivalent to reducing the stiffness of the ice by, for example, increasing its temperature. Also following Schoof (2007), we impose a bed topography with an idealized sill and overdeepening:

$$b = -\left[729 - 2184.8 \times \left(\frac{x}{750\mathrm{km}}\right)^2 + 1031.72 \times \left(\frac{x}{750\mathrm{km}}\right)^4 - 151.72 \times \left(\frac{x}{750\mathrm{km}}\right)^6\right]\mathrm{m}. \qquad (20)$$

Table 3. Scales and parameter values computed using the constants in Table 2

scale/parameter	expression		value	
	using Coulomb Law	using Budd Law	using Coulomb Law	using Budd Law
Q_0	imposed channel discharge scale		$1~\mathrm{m^3~s^{-1}}$	
h_0	imposed ice thickness scale		1000 m	
x_0	imposed glacier length scale		100 km	
ψ_0	$\psi_0 = \rho_w g \frac{h_0}{x_0}$		$101~\mathrm{Pa~m^{-1}}$	
S_0	$S_0 = \left(f\rho_w g \frac{Q_0^2}{\psi_0}\right)^{3/8}$		$2.07~\mathrm{m^2}$	
m_0	$m_0 = \frac{Q_0 \psi_0}{L}$		$3.06 \times 10^{-4}~\mathrm{kg~m^{-1}~s^{-1}}$	
t_{h0}	$t_{h0} = \frac{\rho_i S_0}{m_0}$		3.5×10^6 s	
M_0	$\frac{Q_0}{x_0}$		$1 \times 10^{-5}~\mathrm{m^2~s^{-1}}$	
N_0	$N_0 = (K_0 t_{h0})^{-1/3}$		5.44×10^5 Pa	
u_0	$u_0 = A_s C_C^n N_0^n$	$u_0 = \left(\frac{\rho_i g h_0^2}{(C_B N_0 x_0)}\right)^n$	$2.90 \times 10^{-6}~\mathrm{m~s^{-1}}$	$1.02 \times 10^{-6}~\mathrm{m~s^{-1}}$
t_0	$t_0 = \frac{x_0}{u_0}$		3.44×10^{10} s	9.78×10^9 s
a_0	$\frac{h_0}{t_0}$		$2.90 \times 10^{-8}~\mathrm{m^2~s^{-1}}$	$1.02 \times 10^{-7}~\mathrm{m^2~s^{-1}}$
β	$\beta \equiv \frac{t_{h0}}{t_0}$		1.81×10^{-4}	6.37×10^{-4}
ϵ	$\epsilon \equiv \frac{x_0 m_0}{Q_0 \rho_i}$		0.033	
r	$r \equiv \rho_i / \rho_w$		0.892	
δ	$\delta \equiv \frac{N_0}{x_0 \psi_0}$		0.065	
α	$\alpha \equiv \frac{2 u_0^{1/n}}{\rho_i g A^{1/n} h_{g0} x_0^{1/n}}$		0.010	0.016
γ	$\gamma \equiv \frac{C N_0 x_0}{\rho_i g h_{g0}^2}$	N/A	1.21	N/A

Some constants and parameters are adjusted from values used in the steady-state experiments to generate an initial grounding-line position that is downstream of the over-deepening. Specifically, we use $M = 1 \times 10^{-6}~\mathrm{m^2~s^{-1}}$ and $Q_{\mathrm{in}} = 0.01~\mathrm{m^3~s^{-1}}$ for all transient experiments. We also use $C_C = 0.5$ for T1.C and T2.C. We run these experiments for 5000 years with 100 time steps. To examine the early stages of the evolution, immediately after the perturbation in A, we also run a version of these experiments at a higher temporal resolution for 10 years with 200 time steps. All transient experiments use a spatial grid of 100 grid points across 85% of the ice domain and 600 grid points for the remaining domain to resolve the boundary layer. The hydrology grid is evenly spaced across 1000 grid points. These adjusted grid resolutions are described in Table 1, and the adjusted constants and parameters are described in Table 2.

In T1, we preserve all points of coupling in our model and observe the modelled grounding-line retreat after perturbing A. In T2, we examine the impact of assuming static (unvarying in time) basal conditions on modelled grounding line retreat. To do this, we eliminate the hydrology equations from the model and represent the static basal hydrology properties with an
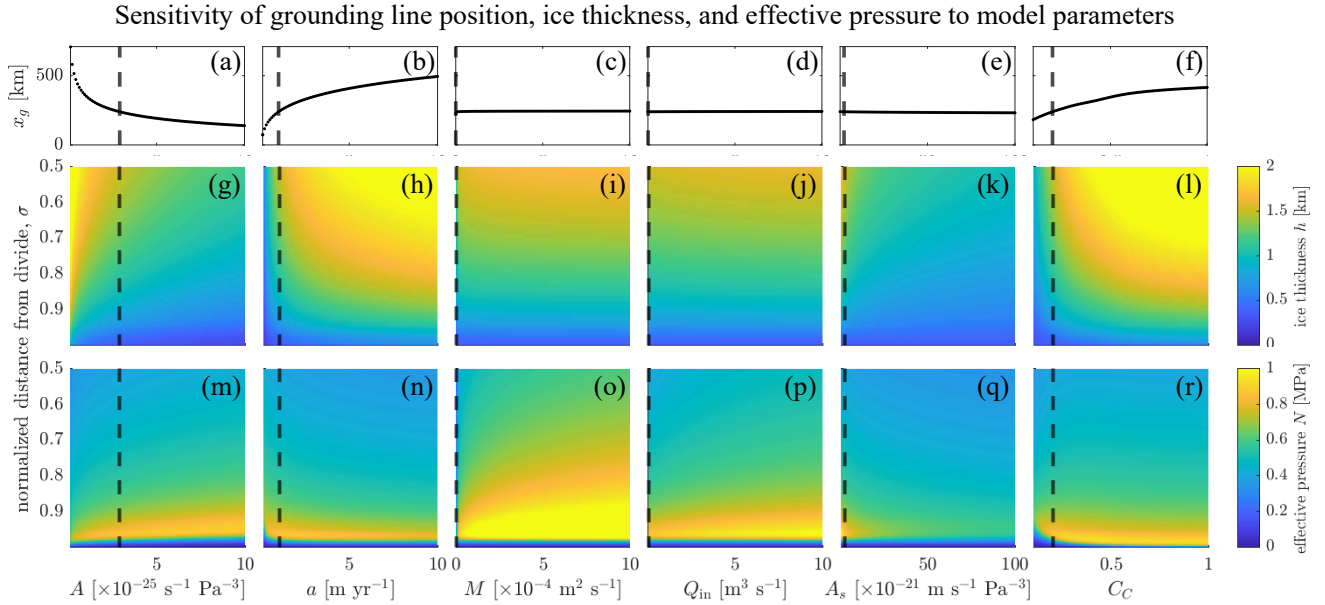
Figure 2. The sensitivity of the coupled model steady state with a regularized Coulomb law to (each column, from left to right) the depth-averaged flow law constant A, the accumulation rate a, the additional water source term M, the water flux at the divide Q_{in}, and the sliding-law-specific constants A_s and C_C. The top row (a-f) shows the steady-state grounding line position, the middle row (g-l) shows the ice thickness h, while the bottom row (m-r) shows the effective pressure N. The parameter values held constant in the other experiments are marked by the dashed black lines.

unchanging effective pressure profile that is used in the basal shear stress term in Eq. (2). To define N, we use values from the initial steady-state solutions of the coupled models in T1. This means that the initial ice-sheet profiles in T1 and T2 are identical. However, unlike experiments in T1, which allow the hydrology to evolve actively with the ice after a perturbation to A, experiments in T2 hold the effective pressure profile static in time. This emulates the approach, common in ice-sheet

245 modelling, of deriving bed parameters with inverse methods and keeping them constant in time. Note that we still use Eq. (3) as a boundary condition on u, so the assumption of $N = 0$ inherent in that expression remains.

3 Results

3.1 Steady-state experiments

Figure 2 shows steady-state grounding line positions, ice thickness profiles, and effective pressure profiles computed with the

250 coupled model with the regularized Coulomb law, for many values of A, a, M, Q, and the friction-law-specific parameters A_s and C_C. In all cases, the grounding line reaches a stable position and the ice thickness decreases monotonically from the divide to the grounding line (note that Fig. 2 only shows the downstream half of the domain). The effective pressure profiles are more
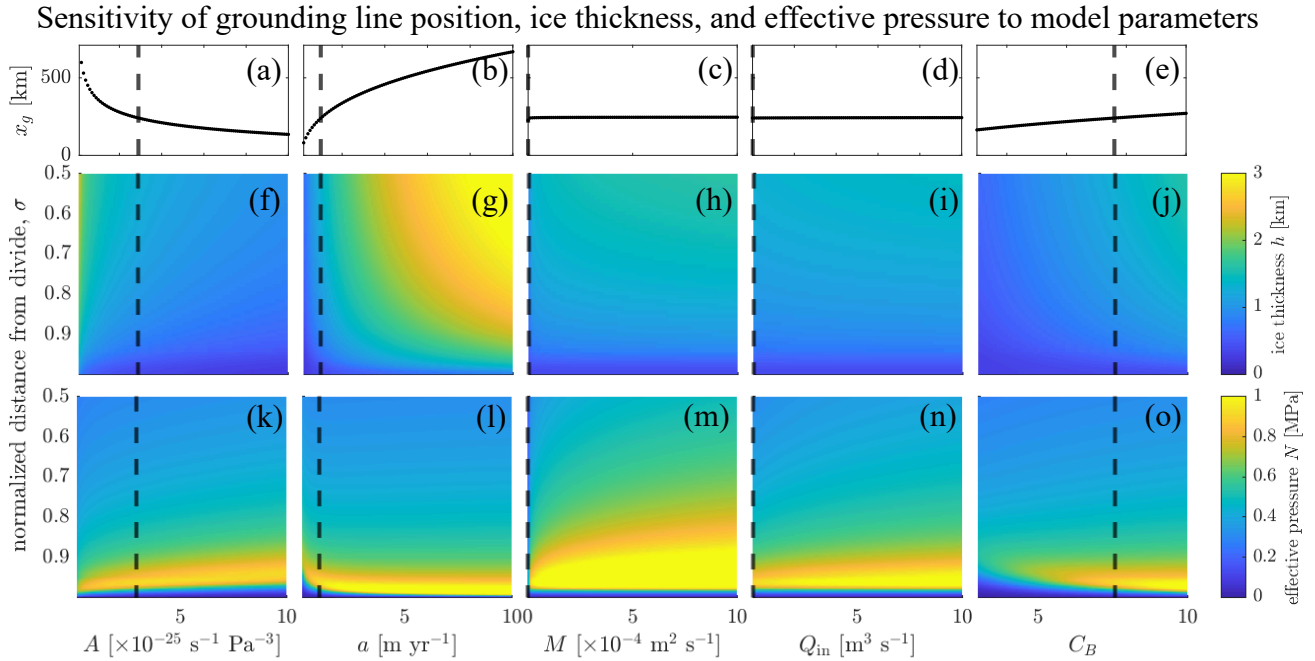
Figure 3. The sensitivity of the coupled model steady state with a Budd law to (each column, from left to right) the depth-averaged flow law constant A, the accumulation rate a, the additional water source term M, and the water flux at the divide Q_{in}, and the sliding-law-specific constant C_B. The top row (a-e) plots the steady-state grounding line position, the middle row (f-j) plots the ice thickness h, while the bottom row (k-o) plots the effective pressure N. The parameter values held constant in the other experiments are marked by the dashed black lines.

complex. A ubiquitous feature in the effective pressure profiles is a maximum that forms relatively close to the grounding line. The positions and magnitudes of the effective-pressure maxima, the grounding line positions, and the ice thickness profiles

255 depend to varying degrees on the five model parameters varied between simulations.

Increasing the ice flow parameter, A, moves the steady-state grounding line position upstream (corresponding to thinner ice at the grounding line), reduces the ice surface slope, and causes a higher peak in effective pressure. Increasing a moves the grounding line downstream (corresponding to thicker ice at the grounding line), and reduces the maximum effective pressure. Increasing the channel source term M or the influx of water at the divide Q_{in} results in slightly thicker ice, significantly

260 larger effective pressures, and minimal ($< 8.4\%$, $< 1\%$, for M, Q_{in}, respectively) changes in grounding-line position. For the regularized Coulomb law parameters, increasing A_s results in thinner ice with a lower maximum effective pressure, and does not impact the grounding line position substantially ($< 3.5\%$). Increasing C_C moves the grounding line downstream, results in thicker ice, and, when $C_C \gtrsim 0.4$, decreases the maximum effective pressure. When $C_C \lesssim 0.4$, decreasing C_C also decreases the maximum effective pressure and the gradient in effective pressure adjacent to the grounding line.
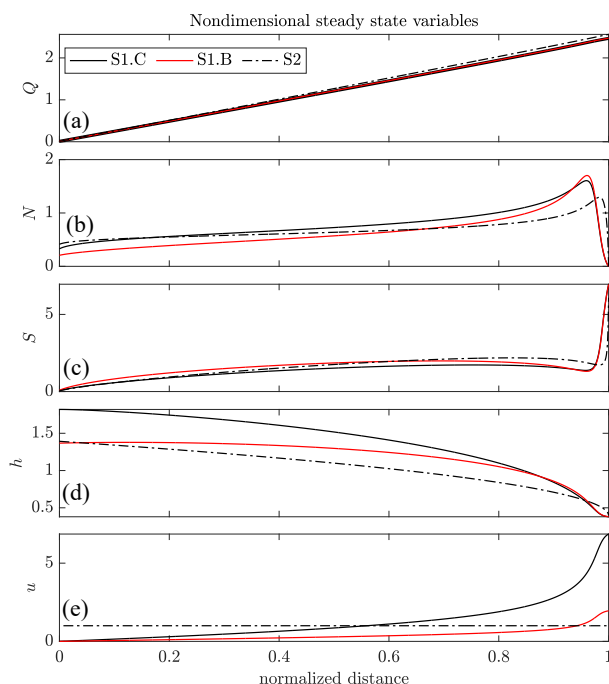
Figure 4. The nondimensional steady-state profiles for: (a) channel discharge, (b) effective pressure, (c) channel cross-sectional area, (d) ice thickness, and (e) ice velocity. The results of the coupled simulations with the regularized Coulomb law (S1.C) are in black, the results from simulations using the Budd law (S1.B) are in red, and the results from the one-way coupled model with imposed thickness and velocity (S2) are in black dash-dotted curves. The location of this simulation in parameter space is indicated by the vertical dashed lines in Fig. 2. Results from S1.C and S1.B exhibit near overlap in (a).

265   Figure 3 displays the parameter sensitivities of the model while using a Budd sliding law. Changes to A and a result in similar changes to x_g, h, and N as described above for the model with the Coulomb sliding law. Increasing the Budd sliding law parameter C_B causes the grounding line to move downstream, an increase in ice thickness, and an increase in effective pressure. While our focus is not the intercomparison of models with different sliding laws (e.g., Brondex et al., 2017), we note that sliding law choice does not change the general trends in model sensitivity to A, a, M, or Q. Regardless of the sliding law

270   or parameter values, the effective pressure profile peaks near the grounding line, and has a steep drop to zero at the grounding line. This steep gradient in N plays an important role in our transient experiments, so we turn to Experiments S1 and S2 to examine this feature further.

     Figure 4 shows the five key nondimensional steady-state model variables from S1.B and S1.C, which use the Coulomb and Budd sliding laws respectively, and our one-way forcing experiment S2, which use an imposed ice thickness h and flow speed

275   u. We note that the grounding line position results on the high-resolution grid differ from those on the low-resolution split grid used in the sensitivity experiments by $< 0.5\%$ for both S1.B and S1.C.

Examining first the results from experiments S1.B and S1.C, Q increases downstream (from left to right in Fig. 4a). The effective pressure N gradually increases downstream before peaking near $x = 0.96$, then steeply decreasing towards the imposed $N = 0$ boundary condition at x_g. Between the peak in N and x_g, N passes an inflection point near $x = 0.98$. This means

280   that the most negative effective pressure gradient is located upstream of the grounding line. The channel cross-sectional area S gradually increases downstream from the divide before reaching a maximum, then decreasing downstream and reaching a minimum near $x = 0.96$, and finally steeply increasing towards x_g. We also see that S exhibits an inflection point approaching x_g near $x = 0.99$, where its curvature changes sign from positive upstream to negative downstream. The ice thickness h decreases monotonically with x, while its gradient increases in magnitude for most of the domain until near the grounding line, where

285   it passes an inflection point near $x = 0.96$ and the gradient begins to decrease in magnitude, approaching zero at x_g. The ice velocity u has an inverse relationship with h, increasing downstream. Like h, the gradient in u increases in magnitude before reaching an inflection point near $x = 0.96$, then approaching zero at x_g.

The results from S2, with the imposed quadratic geometry, follow similar trends to S1: Q increases monotonically, S decreases gradually with x then increases steeply towards x_g, and N increases downstream from the divide before peaking then

290   decreasing rapidly to zero at x_g. The main difference is that these variables do not have points of inflection around $x = 0.96$ as seen in the results from the coupled model (S1). This highlights how the ice surface topography controls the hydrology: the ice geometry in the coupled experiments exhibits an inflection point and this is reflected in the hydrology profiles, whereas the quadratic ice geometry (Eq. 19) does not, and hence when this is used to drive the hydrological part of the model, the results also lack these inflection points.

295   For each of the three experiments (S1.B, S1.C and S2), Fig. 5 shows the nondimensional values of each term in Eqs. (12, 14, 16) to further illustrate how the ice and the hydrology influence one another. In the first column, we see the small but important effect of ice flow advecting the subglacial channel. We anticipated this term to be small, as $\beta \ll 1$. However, across the three experiments, as N approaches zero at the grounding line, creep closure (SN^3 in Eq. 12) also approaches zero, as illustrated by the red dashed curves in Fig. 5. In the absence of advection, this would need to be accommodated by a reduction in the

300   melt term $\frac{|Q|^3}{S^{8/3}}$. Given that $Q > 0$, this would require S to grow to infinity. We see from the steady-state profile in Fig. 4c that S grows large, but does not grow to infinity, and that is due to the advection term growing near the boundary, contributing to channel closure (because $\frac{\partial S}{\partial x} > 0$), and therefore helping to balance the non-zero melt (insets, Fig. 5).

The middle column of Fig. 5 explains the relationship between effective pressure and ice geometry. This is most clearly seen in the one-way experiment (S2; Fig. 5h). Consistent with $\delta \ll 1$, for most of the domain $\frac{Q|Q|}{S^{8/3}}$ follows ψ, which is set by

305   the ice geometry and bed topography. However, as we approach x_g, $\frac{Q|Q|}{S^{8/3}}$ and ψ diverge; as we approach the $N = 0$ boundary condition, S grows large and $\frac{Q|Q|}{S^{8/3}}$ approaches zero. In contrast, h growing steeper near the grounding line causes ψ to grow large. To balance this mismatch between the gradient required to drive flow ($\frac{Q|Q|}{S^{8/3}}$) and the hydraulic gradient supplied by the ice geometry (ψ), $\delta \frac{\partial N}{\partial x}$ grows large and negative. This explains the steep decrease in N just upstream of the grounding line (Fig. 5h).

310   The same relationships hold for the results from the coupled experiments (S1), with some modification related to the inflection points induced by the ice geometry, discussed above. In both S1 experiments, the $\frac{Q|Q|}{S^{8/3}}$ drops below ψ near the grounding

14

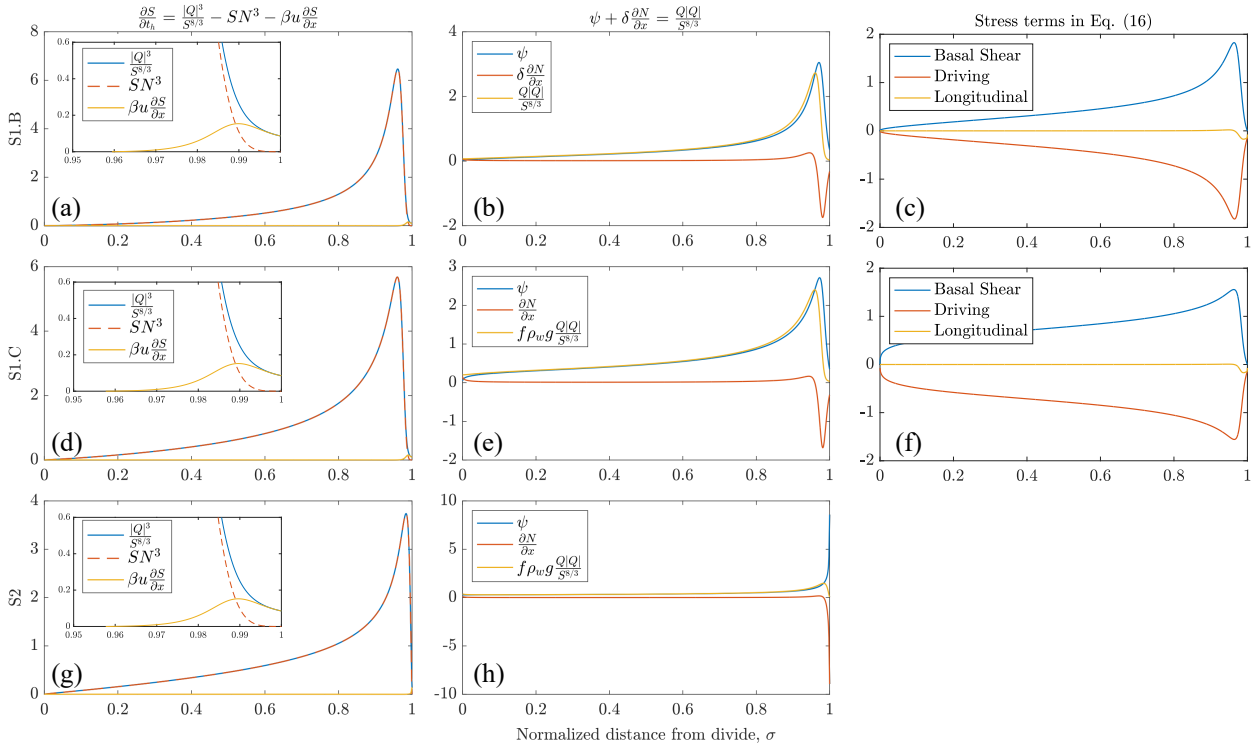Comparing steady state terms in key model equations

Figure 5. The terms in the nondimensional steady-state equation for channel evolution (left column: a, d, g), in the equation for channel conservation of momentum (middle column: b, e, h), and in the equation for ice conservation of momentum (right column: c, f) for the steady-state coupled model solution using a Budd sliding law (top row: a-c), the solution using a regularized Coulomb law (middle row: d-f), and the one-way coupled solution using an imposed quadratic ice geometry (bottom row: g, h).

line, and the difference is made up by a negative $\delta\frac{\partial N}{\partial x}$ (just as in S2). In contrast to the results from S2, an inflection point in the ice thickness influences the hydrology; ψ no longer grows to a maximum at x_g, as it does with the imposed quadratic geometry. Instead, ψ reaches a maximum upstream of the grounding line, causing the effective pressure gradient to reach a

315   minimum slightly upstream of the grounding line (c.f. the red curves in the middle column of Fig. 5). This minimum shows up as a point of inflection in the N profiles for the S1 results that is not seen in the S2 results.

Regardless of the whether the ice and hydrology are fully coupled (S1) or one-way coupled (S2), $\delta\frac{\partial N}{\partial x}$ is negative near the grounding line in response to high ψ in this region. This results in N growing large as you move upstream from the grounding line.

320   Figures 5c and 5f show the steady-state stress balance from S1.B and S1.C. As anticipated (due to $\alpha \ll 1$), the longitudinal stresses are small for the majority of the ice sheet. However, they increase and have more effect near the grounding line where
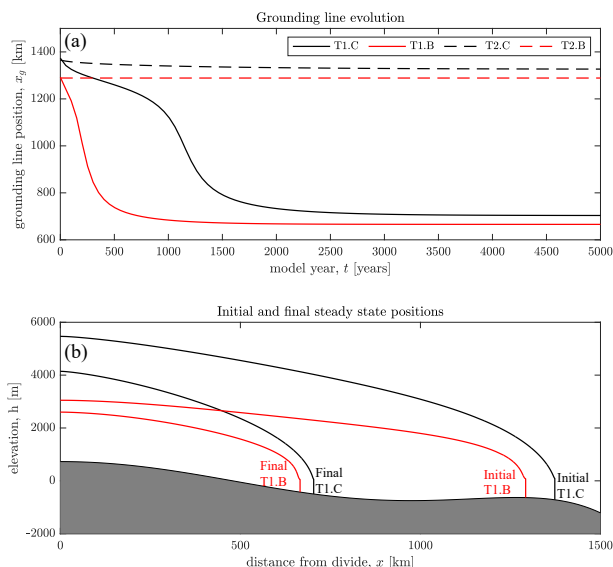
15

Figure 6. (a) The grounding-line position and (b) the initial and final ice-thickness profiles of the coupled model with a regularized Coulomb law (black curves) and a Budd law (red curves) over 5000 years of evolution after a perturbation to A from 0.9×10^{-25} s^{-1}Pa^{-3} to 2.9×10^{-25} s^{-1}Pa^{-3}. The dashed curves show the evolution of the static-N model using a regularized Coulomb law (black curve) and a Budd law (red curve). The upper boundary of lower shaded region is the ice-sheet bed.

the basal shear stress drops to zero. The basal shear stress profiles also illustrate the effect the hydrology has on ice flow, as they mimic the N profiles, particularly near the grounding line.

In summary, regardless of variation in parameters (Figs. 2 and 3), as long as the gradient in ice thickness grows in the downstream direction, the effective pressure grows to a maximum before dropping to zero at the grounding line. This steep negative gradient in N means that regions of much higher effective pressure exist just upstream of the grounding line. This in turn causes a region of higher basal shear stress. Next, we explore the consequences of this high basal shear stress region for grounding line retreat if basal properties are assumed static in time.

3.2 Transient Experiments

The solid curves in Fig. 6 show results from transient simulations using the coupled models with the regularized Coulomb law (T1.C) and the Budd law (T1.B). The ice sheet and hydrological system start in a steady state with the grounding line near the top of the sill, found by solving the fully coupled model in a steady state using an ice flow parameter A of 0.9×10^{-25} s^{-1}Pa^{-3}. The transient simulation starts with A being increased to 2.9×10^{-25} s^{-1}Pa^{-3}, which triggers ice thinning and grounding-line retreat. The grounding line rapidly retreats past the overdeepening to reach a steady state on the upstream prograde slope, a total retreat of about 626 km. In T1.C, the grounding line starts further past the sill, so it takes longer to get over the sill. Once over, it also undergoes rapid retreat of almost 670 km to a steady state on the prograde slope. Looking closely near the
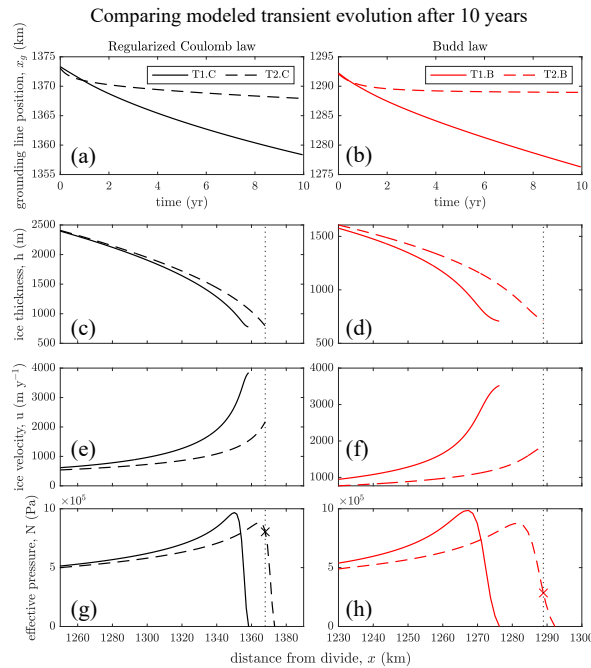
16

Figure 7. The grounding-line position over 10 years of evolution for the coupled model (T1, solid curves) and static-N model (T2, dashed curves) using a (a) regularized Coulomb law (black curves) and (b) Budd law (red curves). The (c,d) ice thickness, (e,f) ice velocity, and (g,h) effective pressure profiles after 10 years of evolution for the models described above. The vertical dotted lines show the position of the static-N grounding lines after 10 years. For the static-N effective-pressure profiles, we plot the initial steady-state profiles and the crosses indicate the effective pressure immediately upstream of the grounding line after 10 years of evolution.

grounding line of the T1 results in Fig. 7 (solid curves, bottom panels), we see the same peak in N and points of inflection in h, u, and N that we saw in the steady-state solutions on the linear bed. This suggests that the relationships between these variables discussed above in relation to the steady-state results also apply on this more complex bed topography and during retreat. Next
340   we compare this coupled evolution with the evolution of an uncoupled ice model that uses a static effective pressure profile.

     Figure 7 and the dashed curves in Figure 6a show results from T2.B and T2.C, where the effective pressure profiles are held static throughout the simulations at their initial values, derived from the fully-coupled solution that provided the initial steady-state conditions. Under these conditions the grounding line, instead of retreating past the overdeepening, approaches a steady-state position on the sill only a relatively small distance upstream of its initial position. In the first ten years of the
345   simulations, the grounding line in T2.B approaches a new steady-state position about 3.5 km upstream of its starting position (Fig. 7a). In T2.C, the grounding line retreats only around 4.75 km in this ten year period (note however that it does not approach a steady state in this time until later in the simulation). This minimal retreat is in stark contrast to the fully coupled experiments (T1), which exhibit faster and larger magnitude grounding line retreat.

We identify the following reasons for these contrasts. In the T2 experiments, the effective pressure is no longer near zero immediately upstream of the terminus during retreat. After the grounding line begins to retreat, the basal shear stress near the terminus grows. The increasing shear stress slows ice flow (c.f. dashed and solid curves in Figs. 7e,f) and prevents further grounding-line retreat. Further retreat results in even higher N values, producing a negative feedback on the ice flow, as the basal shear stress increases further. The coupled model, on the other hand, allows N immediately upstream of the grounding line to remain close to zero as the grounding line retreats; the hydrological system evolves in response to the changing ice geometry to keep N (and therefore basal shear stress) low upstream of the grounding line, which in turn facilitates further retreat.

These differences between the T1 and T2 simulations can also be understood in terms of the ice stress balance, as follows. The instantaneous increase in A reduces the longitudinal stress. Because N is near zero immediately upstream of the grounding line, this reduction in the longitudinal stress forces the driving stress to drop to balance it. The drop in driving stress is accommodated by thinning and subsequent retreat of the grounding line. In contrast, in Experiment T2, when N does not change with time, the higher N near the boundary (and therefore higher basal shear stress) requires a higher driving stress to balance the same perturbation in A, which results in thicker ice and less grounding-line retreat.

4 Discussion

We have developed a model of subglacial hydrology that is bidirectionally coupled to ice flow. In all solutions to the model, the subglacial channel grows large in the region upstream of the grounding line, and an area of high effective pressure forms immediately upstream of this region. These features form independent of whether we use a Budd or regularized Coulomb sliding law. A suite of sensitivity tests shows that the peak in channel size and N occurs across a wide parameter space. An experiment using only one-way coupling between the ice and hydrology shows that imposed ice geometries can produce similar profiles of N. Our plotting of terms in Fig. 5 demonstrates the roles different processes play in the effective-pressure profiles. Next, to further explore what occurs near the grounding line, we create a reduced model for the effective pressure, and show that it cannot apply at the grounding line. We discuss the behaviour of channel size at the grounding line, and comment on how a channel size increase feeds back on the effective pressure.

First, we reduce our coupled model by identifying parameters that are small in our dimensionless equations. δ is small, which means that the flow of water is primarily driven by the basic hydraulic gradient rather than the effective pressure gradient, at least in locations where effective-pressure gradients are not large. ϵ is small, which means that the water flow gradient is mostly influenced by additional water sources along the channel, rather than by melt or creep of the channel walls. As identified earlier, the timescale for ice dynamics is much greater than that of the hydrology, meaning that β is small. Knowing that δ, ϵ, and β

are small, Eqs. (12-14) can be reduced to:

$$N = \frac{Q}{S^{11/9}}, \tag{21}$$

$$\frac{\partial Q}{\partial x} = M, \tag{22}$$

$$S = \frac{Q^{3/4}}{\psi^{3/8}}. \tag{23}$$

Combining Eqs. (21) and (23) gives

$$N = Q^{1/12}\psi^{11/24}, \tag{24}$$

which holds for most of the ice sheet far from the grounding line. Equation (22) indicates that Q increases downstream. Assuming that the bed slope is small ($\frac{\partial b}{\partial x} \ll 1$) and that the ice sheet gets steeper further from the divide, meaning that $-\frac{\partial h}{\partial x}$ grows downstream, Eq. (24) grows downstream from the divide. However, Eq. (24) does not satisfy $N = 0$ at the grounding line. Consequently, a separate near-field solution would be required to describe a boundary layer in N near $x = x_g$. This requires a negative gradient in N within the boundary layer such that the upstream N represented by Eq. (24) will match with the $N = 0$ boundary condition.

The $N = 0$ boundary condition also impacts the channel cross-sectional area, S. As we approach the grounding line, N, and therefore the creep closure term SN^3 in Eq. (12), approach zero. This drop in SN^3 results in the melt-opening term in Eq. (12) dominating, causing the channel cross-sectional area to grow large near the terminus. However, if we consider the steady-state reduced model that applies far from the grounding line, Eq. (21) shows that, for a channel with nonzero water flow, Q, enforcing $N = 0$ requires S to be infinite. This is not physical, so we recognize that the advection term $\beta u \frac{\partial S}{\partial x}$ must grow large near the grounding line. This result highlights the importance of the ice velocity advecting the drainage system, as it allows the coupled model to reach a steady state (see also Drews et al., 2017).

The channel cross-sectional area S growing large at the grounding line in turn facilitates N dropping to zero. Specifically, as discussed in Section 3, a large S results in the right side of Eq. (9) becoming small, which results in the effective pressure gradient approximately equalling the negative of the basic hydraulic gradient, i.e. $\psi \approx -\frac{\partial Q}{\partial x}$. Integrating this expression using the boundary condition $N(x_g) = 0$ yields

$$N \approx -\rho_w g b + \rho_i g h. \tag{25}$$

This expression is consistent with $N = 0$ at the grounding line, because the flotation condition is $\rho_i g h = \rho_w g b$. This expression, which is derived simply by assuming S is large, thus provides the negative gradient required to bring N to 0 from its far-field solution, as described by Eq. (24). Notably, this result is equivalent to assuming that the hydrology system is hydrostatically connected to the ocean, as done in previous modelling studies (e.g., Tsai et al., 2015; Brondex et al., 2017). The above discussion provides physical justification for this assumption and highlights how this simplification can be justified by the channel cross-sectional area growing large near the grounding line through ice-water coupling.

Consistent with previous work, we find that h and u pass inflection points in the region upstream of the grounding line, with the ice-thickness gradient tapering towards zero at the grounding line. Tsai et al. (2015) examined this feature using an

410   ice-sheet model that assumed full hydrostatic connectivity with a regularized Coulomb law (i.e. basal shear stress was assumed to be proportional to effective pressure near the grounding line). This assumption means that, like in our model, N and τ_b vanished at the grounding line. They showed that these inflection points arise due to the vanishing basal shear stress (Tsai et al., 2015).

     One potential implication of our results is that, in areas with channelized subglacial drainage and relatively steep ice thickness
415   profiles, the region immediately upstream of the grounding line will experience high effective pressure and basal shear stress. Previous models and observations are consistent with such a spatial distribution of basal shear stress. Hayden and Dow (2023) impose a realistic ice geometry on a two-dimensional multi-element subglacial-hydrology model, and their modelled effective pressures show the same abrupt increase in effective pressure immediately upstream of the grounding line that we observe, regardless of whether the water flow is channelized or distributed. McCormack et al. (2022) inferred high basal shear stresses
420   in the downstream region of Thwaites Glacier and find lower basal shear stresses further upstream. While (McCormack et al., 2022) discuss spatial variations in basal roughness (Schroeder et al., 2014) and in drainage-system configuration (Schroeder et al., 2013) as contributors to this spatial pattern, we propose that it could also be explained by coupling between a channelized drainage system and ice flow. Future efforts to discriminate the control that hydrology has on basal friction from other factors will be valuable, particularly considering that the hydrologically controlled component of basal shear can potentially change
425   rapidly (e.g., Das et al., 2008; Joughin et al., 2013).

     Temporal evolution is the focus of our transient experiments. In the steady-state simulations, the ice thickness and velocity control the hydrology more consequentially than the other way around; this is demonstrated by experiment S2, in which we imposed the ice thickness and velocity. The transient experiments, by contrast, highlight the role hydrology can have on the ice. The key takeaway from these experiments—designed to emulate the approach of inverting for bed properties and leaving them unchanged that is used in most larger-scale ice-sheet models—is that holding the hydrology static severely impacts ice
430   flow near the grounding line. In our model, this results in a significant reduction in grounding-line retreat. The evolution of the hydrology system together with the ice facilitates faster, larger-magnitude retreat. This follows results from Brondex et al. (2017), who use velocity and shear-stress profiles determined using a regularized Coulomb law to invert for a sliding parameter C_W in a Weertman sliding law that is held static. Their subsequent simulations with the Weertman sliding law result in minimal
435   grounding-line retreat (Brondex et al., 2017). Inverting for C_W and holding it static is similar to our approach of holding N static. We confirm that this static assumption is what causes the lack of retreat, show that it also applies to Budd and regularized Coulomb sliding laws, and reveal the processes that control N in the region upstream of the grounding line.

     The stark difference in retreat accommodated by the coupled models compared to that of the static-N models has broader implications for larger ice-sheet-modeling efforts. In many state-of-the-art ice-sheet models, it is common to invert for a spa-
440   tially variable basal shear-stress or sliding-law parameter that encompasses all basal variables, subglacial hydrology included, and keep this static in time (e.g., Arthern and Gudmundsson, 2010; Morlighem et al., 2013; Arthern et al., 2015). However, these inversions are based on present-day measurements and holding the resulting bed properties constant does not account for future ice-sheet evolution (Arthern et al., 2015). Some large-scale ice-sheet models evolve basal conditions, but it is done through parameterizations (e.g., Leguy et al., 2021, 2014; Kazmierczak et al., 2022). Our work suggests a physical basis for

445   one approach of assuming perfect hydraulic connectivity, but it is currently uncertain how good an approximation this is, particularly away from the region immediately upstream of the grounding line. This uncertainty emphasizes the need for efforts to better represent subglacial hydrology in ice sheet models.

     Finally, although our coupled model includes the detailed physics of both a subglacial channel and a one-dimensional, marine-terminating ice sheet, it employs many simplifying assumptions. For the ice component, we neglect vertical velocities

450   and vertical variability in horizontal velocities. We also neglect variation in ice temperature, ice-shelf buttressing effects, and lateral variability in the ice. This means that our model is applicable only to an ice sheet with relatively low basal shear stress and a freely floating ice shelf (no buttressing). Variations in temperature would result in nonuniform A values and alter ice dynamics, and variations at the ice-sheet base could result in ice freezing to the bed or in additional basal melt. For the hydrology component, we model only a single subglacial channel, and do not consider distributed or multi-channel systems.

455   This simplification leads to another assumption that a region of the ice sheet large enough to control the ice dynamics has an effective pressure equal to the channel's effective pressure. Kingslake and Ng (2013)'s results suggests that to a first order, the effective pressure in a distributed linked cavity system connected to a channel follows that of the channel, but this will not be true far from the channel. Our findings may therefore apply only to regions with channelized drainage. Additionally, we assume a uniform and constant supply term M and input term Q_{in}, when in reality the channel could be supplied by spatially and

460   temporally varying sources. We also assume a channel that is formed by incision upwards into the ice, whereas observations and models suggest that channels can also be form by incision downwards into sediments (Ng, 2000; Livingstone et al., 2016). Including these processes in our model, along with sediment deposition (Drews et al., 2017), would significantly impact its behavior. All these considerations make our model unlikely to quantitatively agree with observations, capture seasonal changes in hydrology, or to be applicable in areas where drainage systems change their configuration between distributed and

465   channelized over space and time. Despite these limitations, the model's simplicity allows a more complete understanding of the model's behavior than would be possible if a more comprehensive model were used. This simplicity has allowed us to qualitatively demonstrate, and understand in detail, some of the ways that active subglacial hydrology could impact long-term ice-sheet retreat.

5   Conclusions and Outlook

470 We have developed a model that uses a novel combination of physical coupling points between a marine-terminating ice sheet and a subglacial channel. We allow the ice-sheet geometry to affect the hydraulic potential of our subglacial channel, the ice velocity to advect the drainage system, and the subglacial water pressure to modulate the shear-stress boundary at the ice base using different effective-pressure-dependent sliding laws. We use our model to investigate how these points of coupling can influence ice dynamics, and we examine the implications of the assumption of holding subglacial properties fixed during

475 transient simulations. We find that the coupled ice–hydrology system creates a zone near the grounding line with high effective pressure. We then show that if the hydrology system is not allowed to evolve with the ice, the ice sheet is much less prone to grounding-line retreat, due to retreat into this zone of high effective pressure. In Section 4, we use a simplified model to further

illustrate how the high effective-pressure region develops, and how the transition from high to zero effective pressure at the grounding line is coupled with a large increase in channel cross-sectional area. These results clarify the mechanisms underlying

480 the stark differences in ice-sheet retreat between our transient experiments and between experiments done by others using different sliding laws (Brondex et al., 2017). Our simplified model analysis also provides a physical basis for the assumption of full hydrologic connectivity to the ocean for regions near the grounding line. Despite limitations to our approach related to the simplifying assumptions discussed in Section 4, our findings highlight how potentially important actively evolving subglacial hydrological systems could be for marine-terminating ice-sheet stability.

485 Our model limitations serve as motivation for future work to incorporate more physics into similar models, such that they can apply to greater range of settings. A first next step is including additional drainage elements, especially since a channel only occupies a limited portion of the bed and the pressure in the channel may not accurately represent pressures across large areas of the bed. Adding additional subglacial hydrology elements such as a coupled channel-cavity system would better represent the full subglacial hydrology environment and could facilitate resolving seasonal effects (e.g., Pimentel et al., 2010; Kingslake

490 and Ng, 2013; Hewitt, 2013). Another step is including additional points of coupling between the ice and hydrology models, for example, basal frictional melting that is a function of basal sliding and influences water flux in the drainage system (Hoffman and Price, 2014). Additional areas of investigation could include coupling the model with geothermal heat flux (Smith-Johnsen et al., 2020), tidal forcing at the grounding line (Rosier et al., 2015), or groundwater aquifer flow and deformation (e.g., Li et al., 2022; Robel et al., 2023).

495 *Code availability.* The code for the model and figures in this manuscript is found here: https://github.com/glugeorge/coupled_ice_hydrology

Appendix A: Additional model details

A1 Nondimensionalization

In the following the scaling of the hydrology equations broadly follows Fowler (1999) and Kingslake (2013). The scaling of the ice-sheet equation follows a similar approach. From Eqs. (1), (2), (7)-(10), we define the following scales:

$$S = S_0 S', t = t_0 t', t_h = t_{h0} t', m = m_0 m', N = N_0 N', u = u_0 u', x = x_0 x', Q = Q_0 Q',$$

$$M = M_0 M', \psi = \psi_0 \psi', h = h_0 h', b = h_0 b', a = a_0 a'.$$

We use the same scale for b and h. Replacing the variables in Eq. (7) with their corresponding scales multiplied by their dimensionless variables from above and setting the first three coefficients equal yields

$$\frac{S_0}{t_{h0}} = \frac{m_0}{\rho_i} = K_0 S_0 N_0^3, \tag{A1}$$

which results in $N_0 = (K_0 t_{h0})^{-1/3}$ and $t_{h0} = \frac{\rho_i S_0}{m_0}$. Setting $\beta = u_0 \frac{t_{h0}}{x_0}$ gives the nondimensional version of Eq. (7):

$$\frac{\partial S'}{\partial t'_h} = m' - S' N'^3 - \beta u' \frac{\partial S'}{\partial x'}. \tag{A2}$$

Replacing the dimensional variables in Eq. (8) gives

$$\frac{S_0}{t_{h0}} \frac{\partial S'}{\partial t'_h} + \frac{Q_0}{x_0} \frac{\partial Q'}{\partial x'} = \frac{m_0}{\rho_i} r m' + M_0 M', \tag{A3}$$

where $r = \rho_i / \rho_w$. Substituting $t_{h0} = \frac{\rho_i S_0}{m_0}$, we obtain

$$\frac{m_0}{\rho_i} \frac{\partial S'}{\partial t'_h} + \frac{Q_0}{x_0} \frac{\partial Q'}{\partial x'} = \frac{m_0}{\rho_i} r m' + M_0 M'. \tag{A4}$$

We define $M_0 = \frac{Q_0}{x_0}$ and the nondimensional parameter $\epsilon \equiv \frac{x_0 m_0}{Q_0 \rho_i}$, yielding the nondimensional form of Eq. (8):

$$\epsilon \frac{\partial S'}{\partial t'_h} + \frac{\partial Q'}{\partial x'} = \epsilon r m' + M'. \tag{A5}$$

We nondimensionalize ψ using Eq. (11), and choose $\psi_0 = \rho_w g \frac{h_0}{x_0}$. Replacing the dimensional variables in Eq. (9) gives

$$\psi_0 \psi' + \frac{N_0}{x_0} \frac{\partial N'}{\partial x'} = f \rho_w g \frac{Q_0^2}{S_0^{8/3}} \frac{Q'|Q'|}{S'^{8/3}}, \tag{A6}$$

which we use to define $S_0 = \left(f \rho_w g \frac{Q_0^2}{\psi_0} \right)^{3/8}$ and $\delta \equiv \frac{N_0}{x_0 \psi_0}$. This gives the nondimensional form of Eq. (9):

$$\psi' + \delta \frac{\partial N}{\partial x} = \frac{Q'|Q'|}{S'^{8/3}}. \tag{A7}$$

Replacing the dimensional variables in Eq. (10) and equating the left side with first term on the right defines

$$m_0 = \frac{Q_0 \psi_0}{L} \tag{A8}$$

23

and yields the nondimensional form of Eq. (10):

$$m' = Q'\left(\psi' + \delta\frac{\partial N'}{\partial x'}\right). \tag{A9}$$

Turning to the ice flow equations, replacing the dimensional variables in Eq. (1) gives

$$\frac{h_0}{t_0}\frac{\partial h'}{\partial t'} + \frac{h_0 u_0}{x_0}\frac{\partial(h'u')}{\partial x'} = a_0 a'. \tag{A10}$$

We set $t_0 = \frac{x_0}{u_0}$. A balance of the accumulation flux with ice-flow over the grounding line leads to $a_0 x_0 = u_0 h_0$. Combining these two expressions leads to $a_0 = \frac{h_0}{t_0}$. And these expressions for t_0 and a_0 lead to the nondimensional version of Eq. (1):

$$\frac{\partial h'}{\partial t'} + \frac{\partial(h'u')}{\partial x'} = a'. \tag{A11}$$

The nondimensionalization of Eq. (2) differs slightly depending on which sliding law we use; the ice velocity scale, u_0, is different in each case. Replacing the dimensional variables in Eq. (2) using the regularized Coulomb sliding law, $\tau_b = C_C N\left(\frac{u}{u+A_s C_C^n N^n}\right)^{1/n}$, gives

$$2\bar{A}^{-1/n}\frac{h_0 u_0^{1/n}}{x_0^{1/n+1}}\frac{\partial}{\partial x'}\left[h'\left|\frac{\partial u'}{\partial x'}\right|^{1/n-1}\frac{\partial u'}{\partial x'}\right] - C_C N_0 N'\left(\frac{u_0 u'}{u_0 u' + A_s C^n N_0^n N'^n}\right)^{1/n} - \rho_i g\frac{h_0^2}{x_0}h'\frac{\partial(h'-b')}{\partial x'} = 0. \tag{A12}$$

Defining $u_0 = A_s C^n N_0^n$, $\alpha = \frac{2u_0^{1/n}}{\rho_i g A^{1/n}h_0 x_0^{1/n}}$, $\gamma = \frac{C_C N_0 x_0}{\rho_i g h_0^2}$, the nondimensional version of Eq. (2) is

$$\alpha\frac{\partial}{\partial x'}\left[h'\left|\frac{\partial u'}{\partial x'}\right|^{1/n-1}\frac{\partial u'}{\partial x'}\right] - \tau_b' - h'\frac{\partial(h'-b')}{\partial x'} = 0, \tag{A13}$$

where $\tau_b' = \gamma N'\left(\frac{u'}{u'+N'^n}\right)^{1/n}$. Alternatively, when using the Budd sliding law, $\tau_b = C_B N^q u^{1/n}$, replacing the dimensional variables in Eq. (2) yields

$$2\bar{A}^{-1/n}\frac{h_0 u_0^{1/n}}{x_0^{1/n+1}}\frac{\partial}{\partial x'}\left[h'\left|\frac{\partial u'}{\partial x'}\right|^{1/n-1}\frac{\partial u'}{\partial x'}\right] - C_B N_0 N' u_0^{1/n} u'^{1/n} - \rho_i g\frac{h_0^2}{x_0}h'\frac{\partial(h'-b')}{\partial x'} = 0. \tag{A14}$$

Dividing through by $\rho_i g\frac{h_0^2}{x_0}$ and setting $u_0 = \left(\frac{\rho_i g h_0^2}{C_B N_0 x_0}\right)^n$ allows α to remain the same as when using a regularized Coulomb law, so the nondimensional equation remains Eq. (A13), where $\tau_b' = N' u'^{1/n}$.

We have now nondimensionalized all the equations. We assign values to Q_0, x_0, and h_0, from which we determine the remaining scales:

$$S_0 = \left(f\rho_w g\frac{Q_0^2}{\psi_0}\right)^{3/8}, t_0 = \frac{x0}{u0}, t_{h0} = \frac{\rho_i S_0}{m_0}, m_0 = \frac{Q_0\psi_0}{L}, \psi_0 = \rho_w g\frac{h_0}{x_0},$$

$$N_0 = (K_0 t_{h0})^{-1/3}, u_0 = A_s C^n N_0^n, M_0 = Q_0/x_0, a_0 = \frac{h_0}{t_0}.$$

Additionally, we have five nondimensional parameters:

$$\epsilon \equiv \frac{x_0 m_0}{Q_0\rho_i}, \delta \equiv \frac{N_0}{x_0\psi_0}, \beta \equiv t_{h0}/t_0, \alpha \equiv \frac{2u_0^{1/n}}{\rho_i g A^{1/n}h_0 x_0^{1/n}}, \gamma \equiv \frac{C N_0 x_0}{\rho_i g h_0^2}.$$

To re-arrange the hydrology equations into 3 equations for our solver, we first take Eqs. (A7) and (A9) and combine to get $m' = \frac{|Q'|^3}{S'^{8/3}}$. Then substituting into Eq. (A2), we get

$$\frac{\partial S'}{\partial t'_h} = \frac{|Q'|^3}{S'^{8/3}} - S'N'^3 - \beta u' \frac{\partial S'}{\partial x'}. \tag{A15}$$

540   Then, subbing this into Eq. (A5), we get our equation for $\frac{\partial Q'}{\partial x'}$:

$$\frac{\partial Q'}{\partial x'} = \epsilon(r-1)\frac{|Q'|^3}{S'^{8/3}} + \epsilon\left(S'N'^3 + \beta u'\frac{\partial S'}{\partial x'}\right) + M'. \tag{A16}$$

Finally, re-arranging Eq. (A7) for $\frac{\partial N'}{\partial x'}$ provides the third hydrology equation:

$$\frac{\partial N'}{\partial x'} = \frac{1}{\delta}\left(\frac{Q'|Q'|}{S'^{8/3}} - \psi'\right). \tag{A17}$$

A2   Coordinate Stretching

545   For the ice flow equations, we use the same coordinate stretching as Appendix A in Schoof (2007). We also apply the same coordinate stretching to the hydrology equations, which are solved on a uniform grid that stretches with the grounding line. Using $\sigma x_g = x$ and $\tau = t_h$, we find that $\frac{\partial}{\partial x}$ and $\frac{\partial}{\partial t_h}$ transform into $\frac{1}{x_g}\frac{\partial}{\partial \sigma}$ and $\frac{\partial}{\partial \tau} - \frac{\sigma}{x_g}\frac{\partial x_g}{\partial \tau}\frac{\partial}{\partial \sigma}$, respectively. Applying these coordinate transformations to the three hydrology equations gives

$$\frac{\partial S'}{\partial \tau} = \frac{|Q'|^3}{S'^{8/3}} - S'N'^3 + \frac{1}{x_g}\left(\sigma\frac{\partial x_g}{\partial \tau} - \beta u'\right)\frac{\partial S'}{\partial \sigma}, \tag{A18}$$

550    $$\frac{1}{x_g}\frac{\partial Q'}{\partial \sigma} = \epsilon(r-1)\frac{|Q'|^3}{S'^{8/3}} + \epsilon\left(S'N'^3 + \frac{\beta u'}{x_g}\frac{\partial S'}{\partial \sigma}\right) + M', \tag{A19}$$

$$\frac{\partial N'}{\partial \sigma} = \frac{x_g}{\delta}\left(\frac{Q'|Q'|}{S'^{8/3}} - \psi'\right). \tag{A20}$$

A3   Discretizing hydrology equations

We follows the method described in Appendix A of Schoof (2007) to discretize and solve the ice-flow equations. We follow a similar approach to discretize and solve the hydrology equations. We use centered differences for the spatial derivatives and

555   forward differences for the time derivatives. The discrete equations are as follows:

$$\frac{S_i^j - S_i^{j-1}}{\Delta\tau} = \frac{|Q_i^j|^3}{S_i^{j8/3}} - S_i^j N_i^{j3} + \frac{1}{x_g^j}\left(\sigma_i^j\frac{x_g^j - x_g^{j-1}}{\Delta\tau} - \beta u_i^j\right)\frac{S_{i+1/2}^j - S_{i-1/2}^j}{2\Delta\sigma}, \tag{A21}$$

$$\frac{1}{x_g^j}\frac{Q_{i+1/2}^j - Q_{i-1/2}^j}{2\Delta\sigma} = \epsilon(r-1)\frac{|Q_i^j|^3}{S_i^{j8/3}} + \epsilon\left(S_i^j N_i^{j3} + \beta u_i^j\frac{S_{i+1/2}^j - S_{i-1/2}^j}{2x_g^j\Delta\sigma}\right) + M', \tag{A22}$$

$$\frac{\delta}{x_g^j}\frac{N_{i+1/2}^j - N_{i-1/2}^j}{2\Delta\sigma} = \frac{Q_i^j|Q_i^j|}{S_i^{j8/3}} - \psi_i^j, \tag{A23}$$

where i subscripts denote the grid point number and j superscripts denote the time step number.

560 *Author contributions.* GL and JK initiated the study. GL led the modeling and writing, and JK advised on and contributed ideas to the model and discussion in addition to helping to write the manuscript.

Competing interests. The authors declare no competing interests.

References

Arnold, N. and Sharp, M.: Flow variability in the Scandinavian ice sheet: modelling the coupling between ice sheet flow and hydrology, Quaternary Science Reviews, 21, 485–502, https://doi.org/10.1016/S0277-3791(01)00059-2, 2002.

Arthern, R. J. and Gudmundsson, G. H.: Initialization of ice-sheet forecasts viewed as an inverse Robin problem, Journal of Glaciology, 56,
575   527–533, https://doi.org/10.3189/002214310792447699, publisher: Cambridge University Press, 2010.

Arthern, R. J. and Williams, C. R.: The sensitivity of West Antarctica to the submarine melting feedback, Geophysical Research Letters, 44, 2352–2359, https://doi.org/10.1002/2017GL072514, _eprint: https://onlinelibrary.wiley.com/doi/pdf/10.1002/2017GL072514, 2017.

Arthern, R. J., Hindmarsh, R. C. A., and Williams, C. R.: Flow speed within the Antarctic ice sheet and its controls inferred from satellite observations, Journal of Geophysical Research: Earth Surface, 120, 1171–1188, https://doi.org/10.1002/2014JF003239, _eprint:
580   https://onlinelibrary.wiley.com/doi/pdf/10.1002/2014JF003239, 2015.

Barnes, J. M. and Gudmundsson, G. H.: The predictive power of ice sheet models and the regional sensitivity of ice loss to basal sliding parameterisations: a case study of Pine Island and Thwaites glaciers, West Antarctica, The Cryosphere, 16, 4291–4304, https://doi.org/10.5194/tc-16-4291-2022, publisher: Copernicus GmbH, 2022.

Bartholomew, I., Nienow, P., Mair, D., Hubbard, A., King, M. A., and Sole, A.: Seasonal evolution of subglacial drainage and acceleration
585   in a Greenland outlet glacier, Nature Geoscience, 3, 408–411, https://doi.org/10.1038/ngeo863, number: 6 Publisher: Nature Publishing Group, 2010.

Bindschadler, R.: The Importance of Pressurized Subglacial Water in Separation and Sliding at the Glacier Bed, Journal of Glaciology, 29, 3–19, https://doi.org/10.3189/S0022143000005104, publisher: Cambridge University Press, 1983.

Brondex, J., Gagliardini, O., Gillet-Chaulet, F., and Durand, G.: Sensitivity of grounding line dynamics to the choice of the friction law,
590   Journal of Glaciology, 63, 854–866, https://doi.org/10.1017/jog.2017.51, publisher: Cambridge University Press, 2017.

Budd, W. F., Keage, P. L., and Blundy, N. A.: Empirical Studies of Ice Sliding, Journal of Glaciology, 23, 157–170, https://doi.org/10.3189/S0022143000029804, publisher: Cambridge University Press, 1979.

Bueler, E. and Brown, J.: Shallow shelf approximation as a "sliding law" in a thermomechanically coupled ice sheet model, Journal of Geophysical Research: Earth Surface, 114, https://doi.org/10.1029/2008JF001179, _eprint:
595   https://onlinelibrary.wiley.com/doi/pdf/10.1029/2008JF001179, 2009.

Chow, V. T.: Open-channel Hydraulics, Blackburn Press, google-Books-ID: JAj7swEACAAJ, 1959.

Clarke, G. K.: Subglacial Processes, Annual Review of Earth and Planetary Sciences, 33, 247–276, https://doi.org/10.1146/annurev.earth.33.092203.122621, _eprint: https://doi.org/10.1146/annurev.earth.33.092203.122621, 2005.

Das, S. B., Joughin, I., Behn, M. D., Howat, I. M., King, M. A., Lizarralde, D., and Bhatia, M. P.: Fracture Propagation to the Base of
600   the Greenland Ice Sheet During Supraglacial Lake Drainage, Science, 320, 778–781, https://doi.org/10.1126/science.1153360, publisher: American Association for the Advancement of Science, 2008.

De Fleurian, B., Werder, M. A., Beyer, S., Brinkerhoff, D. J., Delaney, I., Dow, C. F., Downs, J., Gagliardini, O., Hoffman, M. J., Hooke, R. L., Seguinot, J., and Sommers, A. N.: SHMIP The subglacial hydrology model intercomparison Project, Journal of Glaciology, 64, 897–916, https://doi.org/10.1017/jog.2018.78, publisher: Cambridge University Press, 2018.

605   Dow, C. F., Ross, N., Jeofry, H., Siu, K., and Siegert, M. J.: Antarctic basal environment shaped by high-pressure flow through a subglacial river system, Nature Geoscience, 15, 892–898, https://doi.org/10.1038/s41561-022-01059-1, number: 11 Publisher: Nature Publishing Group, 2022.

Drews, R., Pattyn, F., Hewitt, I. J., Ng, F. S. L., Berger, S., Matsuoka, K., Helm, V., Bergeot, N., Favier, L., and Neckel, N.: Actively evolving subglacial conduits and eskers initiate ice shelf channels at an Antarctic grounding line, Nature Communications, 8, 15 228, https://doi.org/10.1038/ncomms15228, number: 1 Publisher: Nature Publishing Group, 2017.

Flowers, G. E.: Modelling water flow under glaciers and ice sheets, Proceedings of the Royal Society A: Mathematical, Physical and Engineering Sciences, 471, 20140 907, https://doi.org/10.1098/rspa.2014.0907, publisher: Royal Society, 2015.

Fountain, A. G. and Walder, J. S.: Water flow through temperate glaciers, Reviews of Geophysics, 36, 299–328, https://doi.org/10.1029/97RG03579, _eprint: https://agupubs.onlinelibrary.wiley.com/doi/pdf/10.1029/97RG03579, 1998.

Fowler, A. C.: Breaking the seal at Grímsvötn, Iceland, Journal of Glaciology, 45, 506–516, https://doi.org/10.3189/S0022143000001362, publisher: Cambridge University Press, 1999.

Gagliardini, O. and Werder, M. A.: Influence of increasing surface melt over decadal timescales on land-terminating Greenland-type outlet glaciers, Journal of Glaciology, 64, 700–710, https://doi.org/10.1017/jog.2018.59, publisher: Cambridge University Press, 2018.

Gudmundsson, G. H., Paolo, F. S., Adusumilli, S., and Fricker, H. A.: Instantaneous Antarctic ice sheet mass loss driven by thinning ice shelves, Geophysical Research Letters, 46, 13 903–13 909, https://doi.org/10.1029/2019GL085027, _eprint: https://onlinelibrary.wiley.com/doi/pdf/10.1029/2019GL085027, 2019.

Hayden, A.-M. and Dow, C. F.: Examining the effect of ice dynamic changes on subglacial hydrology through modelling of a synthetic Antarctic glacier, Journal of Glaciology, pp. 1–14, https://doi.org/10.1017/jog.2023.65, publisher: Cambridge University Press, 2023.

Helanow, C., Iverson, N. R., Woodard, J. B., and Zoet, L. K.: A slip law for hard-bedded glaciers derived from observed bed topography, Science Advances, 7, eabe7798, https://doi.org/10.1126/sciadv.abe7798, 2021.

Hewitt, I. J.: Seasonal changes in ice sheet motion due to melt water lubrication, Earth and Planetary Science Letters, 371-372, 16–25, https://doi.org/10.1016/j.epsl.2013.04.022, 2013.

Hoffman, M. and Price, S.: Feedbacks between coupled subglacial hydrology and glacier dynamics, Journal of Geophysical Research: Earth Surface, 119, 414–436, https://doi.org/10.1002/2013JF002943, _eprint: https://onlinelibrary.wiley.com/doi/pdf/10.1002/2013JF002943, 2014.

Iken, A. and Bindschadler, R. A.: Combined measurements of Subglacial Water Pressure and Surface Velocity of Findelengletscher, Switzerland: Conclusions about Drainage System and Sliding Mechanism, Journal of Glaciology, 32, 101–119, https://doi.org/10.3189/S0022143000006936, publisher: Cambridge University Press, 1986.

Joughin, I., Das, S. B., Flowers, G. E., Behn, M. D., Alley, R. B., King, M. A., Smith, B. E., Bamber, J. L., van den Broeke, M. R., and van Angelen, J. H.: Influence of ice-sheet geometry and supraglacial lakes on seasonal ice-flow variability, The Cryosphere, 7, 1185–1192, https://doi.org/10.5194/tc-7-1185-2013, publisher: Copernicus GmbH, 2013.

Kazmierczak, E., Sun, S., Coulon, V., and Pattyn, F.: Subglacial hydrology modulates basal sliding response of the Antarctic ice sheet to climate forcing, The Cryosphere, 16, 4537–4552, https://doi.org/10.5194/tc-16-4537-2022, publisher: Copernicus GmbH, 2022.

Kingslake, J.: Modelling Ice-Dammed Lake Drainage, PhD Thesis, University of Sheffield, Sheffield, United Kingdom, 2013.

Kingslake, J. and Ng, F.: Modelling the coupling of flood discharge with glacier flow during jökulhlaups, Annals of Glaciology, 54, 25–31, https://doi.org/10.3189/2013AoG63A331, publisher: Cambridge University Press, 2013.

Le Brocq, A. M., Payne, A. J., Siegert, M. J., and Alley, R. B.: A subglacial water-flow model for West Antarctica, Journal of Glaciology, 55, 879–888, https://doi.org/10.3189/002214309790152564, publisher: Cambridge University Press, 2009.

Le Brocq, A. M., Ross, N., Griggs, J. A., Bingham, R. G., Corr, H. F. J., Ferraccioli, F., Jenkins, A., Jordan, T. A., Payne, A. J., Rippin,
645   D. M., and Siegert, M. J.: Evidence from ice shelves for channelized meltwater flow beneath the Antarctic Ice Sheet, Nature Geoscience,
        6, 945–948, https://doi.org/10.1038/ngeo1977, number: 11 Publisher: Nature Publishing Group, 2013.

Leguy, G. R., Asay-Davis, X. S., and Lipscomb, W. H.: Parameterization of basal friction near grounding lines in a one-dimensional ice sheet
        model, The Cryosphere, 8, 1239–1259, https://doi.org/10.5194/tc-8-1239-2014, publisher: Copernicus GmbH, 2014.

Leguy, G. R., Lipscomb, W. H., and Asay-Davis, X. S.: Marine ice sheet experiments with the Community Ice Sheet Model, The Cryosphere,
650   15, 3229–3253, https://doi.org/10.5194/tc-15-3229-2021, publisher: Copernicus GmbH, 2021.

Li, L., Aitken, A. R. A., Lindsay, M. D., and Kulessa, B.: Sedimentary basins reduce stability of Antarctic ice streams through groundwater
        feedbacks, Nature Geoscience, 15, 645–650, https://doi.org/10.1038/s41561-022-00992-5, number: 8 Publisher: Nature Publishing Group,
        2022.

Lipscomb, W. H., Leguy, G. R., Jourdain, N. C., Asay-Davis, X., Seroussi, H., and Nowicki, S.: ISMIP6-based projections of ocean-forced
655   Antarctic Ice Sheet evolution using the Community Ice Sheet Model, The Cryosphere, 15, 633–661, https://doi.org/10.5194/tc-15-633-
        2021, publisher: Copernicus GmbH, 2021.

Livingstone, S. J., Utting, D. J., Ruffell, A., Clark, C. D., Pawley, S., Atkinson, N., and Fowler, A. C.: Discovery of relict subglacial lakes and
        their geometry and mechanism of drainage, Nature Communications, 7, ncomms11 767, https://doi.org/10.1038/ncomms11767, number:
        1 Publisher: Nature Publishing Group, 2016.

660 MacAyeal, D. R.: Large-scale ice flow over a viscous basal sediment: Theory and application to ice stream B, Antarc-
        tica, Journal of Geophysical Research: Solid Earth, 94, 4071–4087, https://doi.org/10.1029/JB094iB04p04071, _eprint:
        https://onlinelibrary.wiley.com/doi/pdf/10.1029/JB094iB04p04071, 1989.

McArthur, K., McCormack, F. S., and Dow, C. F.: Basal conditions of Denman Glacier from glacier hydrology and ice dynamics modeling,
        The Cryosphere, 17, 4705–4727, https://doi.org/10.5194/tc-17-4705-2023, publisher: Copernicus GmbH, 2023.

665 McCormack, F. S., Warner, R. C., Seroussi, H., Dow, C. F., Roberts, J. L., and Treverrow, A.: Modeling the Deformation Regime of Thwaites
        Glacier, West Antarctica, Using a Simple Flow Relation for Ice Anisotropy (ESTAR), Journal of Geophysical Research: Earth Surface,
        127, e2021JF006 332, https://doi.org/10.1029/2021JF006332, _eprint: https://onlinelibrary.wiley.com/doi/pdf/10.1029/2021JF006332,
        2022.

Morlighem, M., Seroussi, H., Larour, E., and Rignot, E.: Inversion of basal friction in Antarctica using exact and incomplete adjoints
670   of a higher-order model, Journal of Geophysical Research: Earth Surface, 118, 1746–1753, https://doi.org/10.1002/jgrf.20125, _eprint:
        https://onlinelibrary.wiley.com/doi/pdf/10.1002/jgrf.20125, 2013.

Muszynski, I. and Birchfield, G. E.: A Coupled Marine Ice-Stream – Ice-Shelf Model, Journal of Glaciology, 33, 3–15,
        https://doi.org/10.3189/S0022143000005281, publisher: Cambridge University Press, 1987.

Ng, F. S. L.: Canals under sediment-based ice sheets, Annals of Glaciology, 30, 146–152, https://doi.org/10.3189/172756400781820633,
675   publisher: Cambridge University Press, 2000.

Nye, J. F.: Water Flow in Glaciers: Jökulhlaups, Tunnels and Veins, Journal of Glaciology, 17, 181–207,
        https://doi.org/10.3189/S002214300001354X, publisher: Cambridge University Press, 1976.

Paterson, W. S. B.: 5 - Structure and Deformation of Ice, in: The Physics of Glaciers (Third Edition), edited by Paterson, W. S. B., pp.
        78–102, Pergamon, Amsterdam, https://doi.org/10.1016/B978-0-08-037944-9.50011-X, 1994.

680   Pimentel, S. and Flowers, G. E.: A numerical study of hydrologically driven glacier dynamics and subglacial flooding, Proceedings of the
      Royal Society A: Mathematical, Physical and Engineering Sciences, 467, 537–558, https://doi.org/10.1098/rspa.2010.0211, publisher:
      Royal Society, 2010.

Pimentel, S., Flowers, G. E., and Schoof, C. G.: A hydrologically coupled higher-order flow-band model of ice dynamics with a
      Coulomb friction sliding law, Journal of Geophysical Research: Earth Surface, 115, https://doi.org/10.1029/2009JF001621, _eprint:
685   https://onlinelibrary.wiley.com/doi/pdf/10.1029/2009JF001621, 2010.

Robel, A.: SSAsimpleM, https://github.com/aarobel/SSAsimpleM, original Date: 2020-11-05. https://github.com/aarobel/SSAsimpleM,
      2021.

Robel, A. A., Sim, S. J., Meyer, C., Siegfried, M. R., and Gustafson, C. D.: Contemporary ice sheet thinning drives subglacial groundwater
      exfiltration with potential feedbacks on glacier flow, Science Advances, 9, eadh3693, https://doi.org/10.1126/sciadv.adh3693, publisher:
690   American Association for the Advancement of Science, 2023.

Rosier, S. H. R., Gudmundsson, G. H., and Green, J. a. M.: Temporal variations in the flow of a large Antarctic ice stream controlled by
      tidally induced changes in the subglacial water system, The Cryosphere, 9, 1649–1661, https://doi.org/10.5194/tc-9-1649-2015, publisher:
      Copernicus GmbH, 2015.

Röthlisberger, H.: Water Pressure in Intra- and Subglacial Channels*, Journal of Glaciology, 11, 177–203,
695   https://doi.org/10.3189/S0022143000022188, publisher: Cambridge University Press, 1972.

Schoof, C.: The effect of cavitation on glacier sliding, Proceedings of the Royal Society A: Mathematical, Physical and Engineering Sciences,
      461, 609–627, https://doi.org/10.1098/rspa.2004.1350, publisher: Royal Society, 2005.

Schoof, C.: Ice sheet grounding line dynamics: Steady states, stability, and hysteresis, Journal of Geophysical Research: Earth Surface, 112,
      https://doi.org/10.1029/2006JF000664, _eprint: https://onlinelibrary.wiley.com/doi/pdf/10.1029/2006JF000664, 2007.

700   Schroeder, D. M., Blankenship, D. D., and Young, D. A.: Evidence for a water system transition beneath Thwaites Glacier, West Antarctica,
      Proceedings of the National Academy of Sciences, 110, 12 225–12 228, https://doi.org/10.1073/pnas.1302828110, publisher: Proceedings
      of the National Academy of Sciences, 2013.

Schroeder, D. M., Blankenship, D. D., Young, D. A., Witus, A. E., and Anderson, J. B.: Airborne radar sounding evidence for de-
      formable sediments and outcropping bedrock beneath Thwaites Glacier, West Antarctica, Geophysical Research Letters, 41, 7200–7208,
705   https://doi.org/10.1002/2014GL061645, _eprint: https://onlinelibrary.wiley.com/doi/pdf/10.1002/2014GL061645, 2014.

Seroussi, H., Nowicki, S., Payne, A. J., Goelzer, H., Lipscomb, W. H., Abe-Ouchi, A., Agosta, C., Albrecht, T., Asay-Davis, X., Barthel,
      A., Calov, R., Cullather, R., Dumas, C., Galton-Fenzi, B. K., Gladstone, R., Golledge, N. R., Gregory, J. M., Greve, R., Hattermann, T.,
      Hoffman, M. J., Humbert, A., Huybrechts, P., Jourdain, N. C., Kleiner, T., Larour, E., Leguy, G. R., Lowry, D. P., Little, C. M., Morlighem,
      M., Pattyn, F., Pelle, T., Price, S. F., Quiquet, A., Reese, R., Schlegel, N.-J., Shepherd, A., Simon, E., Smith, R. S., Straneo, F., Sun, S.,
710   Trusel, L. D., Van Breedam, J., van de Wal, R. S. W., Winkelmann, R., Zhao, C., Zhang, T., and Zwinger, T.: ISMIP6 Antarctica: a multi-
      model ensemble of the Antarctic ice sheet evolution over the 21st century, The Cryosphere, 14, 3033–3070, https://doi.org/10.5194/tc-14-
      3033-2020, publisher: Copernicus GmbH, 2020.

Smith-Johnsen, S., Fleurian, B. d., and Nisancioglu, K. H.: The role of subglacial hydrology in ice streams with elevated geothermal heat
      flux, Journal of Glaciology, 66, 303–312, https://doi.org/10.1017/jog.2020.8, publisher: Cambridge University Press, 2020.

715   Tsai, V. C., Stewart, A. L., and Thompson, A. F.: Marine ice-sheet profiles and stability under Coulomb basal conditions, Journal of Glaciol-
      ogy, 61, 205–215, https://doi.org/10.3189/2015JoG14J221, publisher: Cambridge University Press, 2015.

Weertman, J.: On the Sliding of Glaciers, Journal of Glaciology, 3, 33–38, https://doi.org/10.3189/S0022143000024709, publisher: Cambridge University Press, 1957.

Weertman, J.: Stability of the Junction of an Ice Sheet and an Ice Shelf, Journal of Glaciology, 13, 3–11,
720   https://doi.org/10.3189/S0022143000023327, publisher: Cambridge University Press, 1974.

Zoet, L. K. and Iverson, N. R.: A slip law for glaciers on deformable beds, Science, 368, 76–78, https://doi.org/10.1126/science.aaz1183, publisher: American Association for the Advancement of Science, 2020.